

# DEEP CHANDRA OBSERVATION OF THE PULSAR WIND NEBULA POWERED BY THE PULSAR J1846-0258 IN THE SUPERNOVA REMNANT KES 75

C.-Y. NG<sup>1</sup>, P. O. SLANE<sup>2</sup>, B. M. GAENSLER<sup>1,†</sup>, J. P. HUGHES<sup>3</sup>

*Draft version September 16, 2008*

## ABSTRACT

We present the results of detailed spatial and spectral analysis of the pulsar wind nebula (PWN) in supernova remnant Kes 75 (G29.7-0.3) using a deep exposure with Chandra X-ray observatory. The PWN shows a complex morphology with clear axisymmetric structure. We identified a one-sided jet and two bright clumps aligned with the overall nebular elongation, and an arc-like feature perpendicular to the jet direction. We interpret the arc as an equatorial torus or wisp and the clumps could be shock interaction between the jets and the surrounding medium. Spatial modeling of the features with a torus and jet model indicates a position angle  $207^\circ \pm 8^\circ$  for the PWN symmetry axis. The lack of any observable counter jet implies a flow velocity larger than  $0.4c$ . Comparing to an archival observation 6 years earlier, some small-scale features in the PWN demonstrate strong variability: the flux of the inner jet doubles, and the peak of the northern clump broadens and shifts  $2''$  outward. As recently reported from RXTE observations, magnetar-like bursts of the central pulsar occurred coincidentally 7 days before the Chandra exposure. Accompanied with the bursts is a temporary increase in the pulsar flux: during the Chandra observation, the pulsar luminosity is 6 times larger than in quiescent state, and shows substantial spectral softening from  $\Gamma = 1.1$  to 1.9 with an emerging thermal component.

*Subject headings:* pulsars: individual (PSR J1846-0258) — supernovae: individual (Kes 75) — stars: winds, outflows — X-rays: ISM

## 1. INTRODUCTION

Kes 75 (G29.7-0.3) (Kesteven 1968) is a composite supernova remnant (SNR) in our Galaxy that harbors one of the youngest known neutron stars. At the center of the  $3'$  diameter SNR shell, there is a pulsar wind nebula (PWN) powered by the source PSR J1846-0258. In radio frequencies, the VLA and the Berkeley-Illinois-Maryland Association (BIMA) array images show a diffuse SNR shell with a flat spectrum core (Helfand et al. 2003; Bock & Gaensler 2005). X-ray observations with ASCA revealed the thermal and non-thermal spectral components of Kes 75 (Blanton & Helfand 1996). A 37 ks Chandra exposure resolved the shell structure and discovered a neutron star embedded in an axisymmetric PWN with complex morphology (Helfand et al. 2003). The observation also indicated a remarkable coincidence between the X-ray and radio emission. Comparing Spitzer infrared images to deep Chandra observations, Morton et al. (2007) suggested a Wolf-Rayet progenitor for the remnant. At higher energy, the PWN has been detected in soft  $\gamma$ -rays by INTEGRAL (McBride et al. 2008) and in the TeV band by HESS (Djannati-Ataï et al. 2007). The first distance estimate to the source placed it at 19 kpc based on neutral hydrogen absorption measurements (Becker & Helfand 1984), implying very high efficiency with which the pulsar converts its spin-down power into X-ray emission (Helfand et al. 2003). Recently Leahy & Tian (2008)

deduced a new distance estimate of 5.1-7.5 kpc from HI and <sup>13</sup>CO maps, providing a more reasonable pulsar luminosity and remnant size.

The pulsar J1846-0258 was discovered in the X-ray band with timing observations using the Rossi X-ray Timing Explorer (RXTE) (Gotthelf et al. 2000), but remains undetected at radio frequencies (Archibald et al. 2008). The spin period ( $P = 324$  ms) and spin down rate ( $\dot{P} = 7.1 \times 10^{-12}$  s s<sup>-1</sup>) imply a large spin-down luminosity of  $\dot{E} \equiv 3.9 \times 10^{46} \dot{P}/P^3$  erg s<sup>-1</sup> =  $8.1 \times 10^{36}$  erg s<sup>-1</sup>, a high surface magnetic strength  $B \equiv 3.2 \times 10^{19} (P/\dot{P})^{1/2}$  G =  $4.9 \times 10^{13}$  G, and a small characteristic age  $\tau_c \equiv P/2\dot{P} = 720$  yr. The large inferred surface magnetic field is near the values found for pulsars whose emission is magnetically dominated, i.e. the magnetars (Woods & Thompson 2006). Subsequent RXTE monitoring observations indicated a braking index of  $n = 2.65 \pm 0.01$  (Livingstone et al. 2006), implying a spin-down age  $\tau \equiv P/(n-1)\dot{P} = 884$  yr, which makes it one of the youngest known neutron star in our Galaxy (see, Bietenholz & Bartel 2008). Gavril et al. (2008) recently reported 5 short X-ray bursts from the pulsar in 2006, along with temporary changes in the spectral and timing noise properties, suggesting magnetar-like nature of this object. Coincidentally, the deep Chandra observation presented in this study was taken only 7 days after these unprecedented bursts. With the same dataset, Kumar & Safi-Harb (2008) independently reported the increase in the pulsar flux and the softening in its spectrum at this time, as a result of the bursts. We note that the above studies focused on the central pulsar and left unresolved the question of variability in the PWN.

In this paper, we concentrate on the spatial and spectral properties of the PWN in Kes 75 using deep Chan-

Electronic address: ncy@physics.usyd.edu.au

<sup>1</sup> Institute of Astronomy, School of Physics, The University of Sydney, NSW 2006, Australia.

<sup>2</sup> Harvard-Smithsonian Center for Astrophysics, 60 Garden Street, Cambridge, MA 02138, USA.

<sup>3</sup> Department of Physics and Astronomy, Rutgers University, 136 Frelinghuysen Road, Piscataway, NJ 08854, USA.

<sup>†</sup> ARC Federation Fellow

dra observations. Specifically, we investigate the variability in the system by comparing exposures from different epochs. This analysis provides a unique opportunity to study the evolution of a young PWN and its interaction with the environment. The observations and data reduction are described in §2. In §3, we present the spatial analysis of the overall PWN structure. The variabilities of the pulsar and the PWN are studied in §4. The spectral analysis is presented in §5 and in §6 we discuss the interpretations of all the above results.

## 2. OBSERVATIONS AND DATA REDUCTION

Deep Chandra observations of Kes 75 were carried out on Jun 5-12, 2006 in four exposures (Observation IDs [ObsIDs] 6686, 7337, 7338 & 7339) which began 7 days after the first four bursts that were reported by Gavril et al. (2008), and 50 days before the fifth one. The data were taken with the ACIS-S array<sup>5</sup> operating in very faint (VF) timed exposure imaging mode using a custom CCD subarray of 600 rows (frame time=1.8s) in order to reduce the photon pile-up. The total exposure was 155 ks and the pulsar was positioned near the aim point on the S3 chip, which was the only CCD active during the observation. For comparison, we have also reprocessed the archival 37 ks exposure (ObsID 748) observed on Oct 15, 2000 (Helfand et al. 2003), which was carried out in ACIS-S faint TE mode with the full CCD frame (frame time = 3.2s). All data reduction was performed using CIAO 4.0 and CALDB 3.4.2. We started with the level=1 event files, turned off the pixel randomization, and applied the time-dependent gain calibration and charge transfer inefficiency (CTI) correction. We did not apply the background cleaning algorithm for the VF observations, which uses the outer 16 pixels of the  $5 \times 5$  event island to improve discrimination between good events and likely cosmic rays, since this rejects too many real events from the bright source. Examination of the background light curves showed no strong flares during all the observations. Hence, all data are included in the analysis. For imaging analysis, the four individual exposures of the 2006 observation were co-added. We first determined the pulsar position with the task `wavdetect`, then aligned the images accordingly. Assuming the roll angle in the header is correct, we applied only linear shifts for the alignment. Since the amount of shift required is at most 0.5 pixels (i.e.  $\sim 0.2''$ ), which is much smaller than the features we are interested in, the error introduced in the process is negligible. For spectral analysis, spectra were extracted from each individual exposure separately, then a joint fit was performed.

## 3. SPATIAL ANALYSIS

Fig. 1 shows the complex morphology of the PWN. As reported previously by Helfand et al. (2003), the  $\sim 30''$  diameter overall structure is filled with diffuse emission and elongated in the northwest-southeast direction with an obvious symmetry axis. The nebula has a sharp edge in the southeast, but a more diffuse boundary in the north with finger-like protrusions. The PWN shows

small-scale features that resemble those of the Crab nebula (Seward et al. 2006), including bays in the east and west, and a chimney in north. At the center of the PWN, a bright point source at the pulsar position is embedded in a compact nebula and has a one-sided collimated jet-like feature extending  $5''$  to the southwest along the nebula axis. This ‘inner jet’ then fades and connects to a broader ‘outer jet’ before it terminates at a clump  $13''$  southwest of the pulsar. The whole PWN is also cutoff sharply at that point. In the northeast, there is another bright clump about  $6'' \times 4''$  aligned with the jet direction. At the base of this northern clump, an arc-like feature, which runs across the entire nebula, is bisected by the jet. Fig. 1c illustrates all these features and the count profiles of the PWN along different regions are plotted in Fig. 2. In particular, the peaks in Fig. 2a & 2c clearly indicate the arc-like feature.

### 3.1. SPATIAL MODELING

Highly collimated polar jets and equatorial outflows such as tori or wisps in X-ray are commonly found features among young PWN systems (see, Gaensler & Slane 2006; Kargaltsev & Pavlov 2008). Magnetohydrodynamics (MHD) simulations show that a latitude-dependent pulsar wind can lead to Doppler-boosted arcs and jets in the X-ray synchrotron emission (e.g. Del Zanna et al. 2006). Employing a simple model to capture these characteristic features, Ng & Romani (2008) demonstrate a robust way to measure the underlying PWN geometry. For the PWN in Kes 75, the highly collimated jet-like feature and its alignment with the nebula symmetry axis strongly suggest its connection to the pulsar polar outflow. In this scenario, the arc-like feature perpendicular to the jet could be part of a Doppler boosted torus or wisp in the equatorial plane. We have applied the pulsar wind torus fitting scheme described by Ng & Romani (2008) to model the geometry of these features. Our model consists of a point source, a torus and three Gaussian ellipses that represent the compact diffuse nebula surrounding the pulsar, and the jets and clumps on both sides. An energy weighted point spread function (PSF), which is simulated with the Chandra Ray Tracer (ChaRT) and MARX software packages using the source spectrum, was used in the fitting. The PSF also includes the CCD readout trail and the pile-up effects. The ellipses are fixed in size and oriented along the torus symmetry axis, while their intensity and separation are determined by the fit. Additional model parameters include the torus axis position angle  $\Psi$  (from north to east), inclination angle  $\zeta$  between the torus axis and the observer line of sight, radius  $R$ , blur  $\delta$  for the torus profile, post-shock flow velocity  $\beta$ , and the intensity of the point source. The best-fit parameters are determined by maximizing a Poisson-based likelihood function. More details on the modeling and fitting can be found in Ng & Romani (2008). Note that we performed the fit to the 2006 epoch only, in order to avoid any complication from different PSFs and instrumental response between observations.

Fig. 3 shows the best-fit model compared to the data, with the corresponding parameters listed in Table 1. We found that the uncertainties in the fit are dominated by the systematic errors, while the statistical errors are negligible since the source is bright and the deep exposure

<sup>5</sup> The ACIS-S detector has pixel size of  $0.492''$  and a practical detection range of 0.3-10 keV in energy, with spectral resolution from 100 to 250 eV across the energy range (see <http://cxc.harvard.edu/proposer/POG/html/chap6.html>).

provides a high signal-to-noise ratio image. It is obvious that our simple model captures only the characteristic features of the PWN, hence the unmodeled structure contributes to the systematic uncertainties. Following Ng & Romani (2008), we attempted to quantify this term by blanking out the jet regions in the fit (the dotted ellipses in Fig. 3). In addition, we also tried fitting only part of the arc by excising the sectors in Fig. 3, one at a time. The change in the parameters indicates how sensitively the results depend on a particular region, therefore providing an estimate of the systematic errors in the fit which are listed in Table 1. At a distance of 6 kpc, the best-fit radius of the arc has a de-projected physical size of 0.3 pc, which falls between values for the inner and outer tori of the Crab pulsar (Ng & Romani 2008), is a reasonable value for a young PWN. The fitting results also indicate a substantial flux contribution from the compact nebula, and that the northern clump is brighter than the southern one. Given the inclination of the pulsar spin axis determined by the fit, a simple picture of Doppler boosted jets predicts the southern clump to be brighter than the northern one, which is clearly inconsistent with the results.

#### 4. VARIABILITY

The 2006 exposure was started 7 days after the first burst reported by Gavriil et al. (2008) and no bursts have occurred during the observation. The pulsar lightcurve shows no short-term variability in and between the four individual exposures. On the other hand, a comparison to the 2000 exposure reveals a drastic increase in the pulsar flux. Fig. 4 shows the exposure corrected images of the PWN for the two observations. In the second epoch, the pulsar is so bright that the CCD pile-up severely complicates the count rate measurement. Therefore we estimated the flux from the CCD readout trail which is due to the ‘out-of-time images’ during the  $40\mu\text{s}$  frame transfer time from one row to another. We employed a rectangular region of  $3''$  width centered on the trail, and selected regions far away from the PWN to avoid any contamination. We tried different background regions and obtained a net count of  $2.7 \pm 0.3 \text{ cts row}^{-1}$  in 1-8 keV range for the 2006 observation. The uncertainty comes from both the statistical fluctuation and systematic errors due to the background estimate. We tried independent measurements for the northeast and southwest trails, as well as for each individual exposure, and the results are all consistent. Since the readout trail consists of not only counts from the pulsar, but also those from the PWN and SNR background in the same columns, the latter have to be subtracted out. Excluding the central  $3''$  radius from the pulsar, there are  $21 \times 10^3$  total counts (1-8 keV range) in a  $3''$  wide rectangular region covering the whole trail of 600 CCD pixels in length. Of these counts, the above estimate suggests that only  $1.5 \times 10^3$  counts are from the readout artifact and the rest are real events from the PWN, SNR and background. Therefore, for a frame time of 1.8 s, the PWN and SNR contribute a total of  $0.4 \text{ cts row}^{-1}$  to the readout trail, implying an unpiled count rate of  $0.7 \pm 0.1 \text{ cts s}^{-1}$  for the pulsar in 1-8 keV range. Note that this is only an upper limit of the true pulsar flux, due to the contamination by the surrounding compact nebula. This is discussed in the next section. Repeating the same exercise on the first epoch

obtains a pulsar count rate of  $0.2 \pm 0.1 \text{ cts s}^{-1}$ . If the pulsar spectrum and the luminosity of the compact nebula remain unchanged between the epochs, the pulsar flux has to increase by a factor of 3.5 in the 1-8 keV energy band.

The total flux of the PWN shows no physical changes between the epochs. Excluding the central  $3''$  radius, the overall PWN has count rates of 0.59 and  $0.61 \text{ cts s}^{-1}$  in 1-8 keV band for the first and second epochs respectively. The 3% difference is entirely due to the scattering of pulsar counts in the same field-of-view. We generated a model PSF without any pile-up effects, and found that the above region contains 3.5% of the point source counts. Therefore, the increase in the pulsar luminosity can easily explain the excess counts in the PWN.<sup>6</sup>

On the other hand, some small-scale features in the PWN do demonstrate significant variability between the observations. The exposure corrected images in Fig. 4 clearly show the evolution of the northern clump and the brightening of the southern inner jet. In the 2006 data, the northern clump broadens and shows a double peak feature. The count profiles in Fig. 5 indicate that its peak has shifted  $2''$  outward, while the total flux remains similar. The southern inner jet also shows hints of morphological evolution: there is an obvious eastern extension at the end of the jet in the 2006 exposure, but it seems to be absent in the first epoch. Detailed studies of the flux and spectral variations of these features will be presented in the following section.

#### 5. SPECTRAL ANALYSIS

##### 5.1. THE PWN SPECTRUM

To investigate the spatial variation of the PWN spectrum, we divided the PWN into different regions and extracted their spectra using the script `specextract` in CIAO. The source and background regions are shown in Fig. 6. As mentioned, the spectra for the 2006 observation were extracted from the four exposure individually, and then fitted jointly. All the spectral fits in this study were carried out in the 0.5-9 keV energy range using the SHERPA environment. The spectra from different regions were fitted simultaneously with a global column density but different powerlaw indices. Careful examination of each spectrum shows no spectral or flux variation between the exposures in the 2006 observation. The best-fit results are listed in Table 2 with the corresponding uncertainties in the parameters. The uncertainties reported here, as well as for the rest of the paper, are 90% confidence intervals for the projected multi-dimensional values, except for the flux values, which are 1-D errors. The best-fit column density  $N_{\text{H}} = (4.06 \pm 0.07) \times 10^{22} \text{ cm}^{-2}$  obtained from the 2006 observation is consistent with the previous measurements (Helfand et al. 2003; Morton et al. 2007; Kumar & Safi-Harb 2008). Comparing the total flux between the epochs indicates a 3% difference, which is in an excellent agreement with the count rate estimate in the above section.

To determine any spectral variations in the overall PWN between the epochs, we refitted both data sets with the column density fixed at  $N_{\text{H}} = 4.0 \times 10^{22} \text{ cm}^{-2}$ , in order to avoid any possible covariance between  $N_{\text{H}}$  and other spectral parameters. The results are shown in

<sup>6</sup>  $(0.7-0.2) \text{ cts s}^{-1} \times 3.5\% \approx 0.02 \text{ cts s}^{-1}$

Table 2, indicating no systematic changes in the spectral indices between the observations, and the fluctuation is mostly within the measurement uncertainties. On the other hand, the table suggests flux variations in regions 1,2,6,9,12, and 14. In particular, the change in region 6 is introduced by the shift of the northern clump into the region. For region 12, the apparent flux increase is the result of pulsar counts scattered into the region, rather than physical changes. From the same analysis as the above section, we have worked out the expected pulsar flux in the region and found that the value is consistent with the excess flux observed. Moreover, the same exercise on the other regions indicates that the flux variations are likely to be physical, but we note that the total flux of the PWN remains unchanged.

Fig. 6 shows the spectral map of the PWN. The compact nebula at the center has a relatively soft spectrum as compared to the innermost part of many other young PWNe. Also, regions along the symmetry axis are systematically harder than the surrounding emission, and the overall spectrum softens as one progresses to larger scales. To further investigate this variation, we extracted the PWN spectra in annular regions and fitted jointly to different powerlaws with a global  $N_H$ . The result for the 2006 data is plotted in Fig. 7, the one from the 2000 data is very similar. Except for the innermost bin, the spectral index increases monotonically with radius. This trend is commonly observed among PWNe, including the Crab, 3C 58 and G21.5–0.9 (Mori et al. 2004; Slane et al. 2004, 2000; Warwick et al. 2001).

In addition to the overall nebula, we also carried out spectral analysis for the individual PWN features. To allow a direct comparison between the structures, we minimize the nebular contamination by subtracting the background from adjacent regions. The extraction regions for the northern clump, southern clump, inner jet, outer jet and southern clump are shown in Fig. 8. As the northern clump shows a double peak structure in the 2006 observation, we further divided the extraction region to determine any spectral difference from the two peaks. The best-fit spectral parameters with 90% confidence intervals are listed in Table 4. The spectral properties vary substantially between the structures. To check if this could be caused by a variable column density, we tried fitting  $N_H$  in the 2006 observation. However, the lower signal-to-noise ratio of the 2000 data precludes a similar exercise. The outer jet seems to have a harder spectrum than the other regions, if it is real, it could indicate either high energy emission or a larger absorption column density in the region. For the northern clump, we do not find any spectral difference for its two peaks. Also, the powerlaw index and total luminosity of the clump show no significant change between the two epochs. On the other hand, the flux of the inner jet doubles in the 2006 observation, which could not be accounted for by the scattering of the pulsar PSF, since the extraction region is small. Variability in pulsar jets has been observed among many PWN systems, such as the Crab, Vela and B1509–58, with timescales from days to years (Hester et al. 2002; Pavlov et al. 2003; DeLaney et al. 2006). Therefore it is not unexpected to detect variation in the inner jet here, given the two epochs are separated by 6 years, see §6.2 for more discussion. We have tried fitting the clump spectra with thermal models to investigate the

scenario in which the clumps represent a shock interaction between the jets and the surrounding materials. We found that a thermal bremsstrahlung provides the best fit among the thermal models, since there is no obvious emission line feature in the spectra. However, as listed in Table 4, the temperature is not very well constrained and statistically the fit is slightly worse than a simple powerlaw. We are thus inclined to infer the emission as non-thermal as seen in other PWNe.

## 5.2. THE PULSAR SPECTRUM

Although the readout trail of the pulsar is free from pile-up, it is much fainter than the background emission from the PWN and the SNR shell to yield any high quality spectrum for the pulsar. Therefore, the pulsar spectrum was extracted from the central 2'' radius using the script `psextract` with the same background regions shown in Fig. 6. We rebuilt the response matrix files (RMFs) with the tool `mkacisrmf` which corrects for the CTI, and employed the Davis (2001) model in the fitting to account for the CCD pile-up effects. Again, for the 2006 observation, the spectra were extracted from individual exposure and then fitted jointly. We did not attempt to fit the column density, as this could be complicated by the pile-up effects and by any possible thermal emission from the pulsar. Instead, it was fixed at the PWN value  $N_H = 4.0 \times 10^{22} \text{ cm}^{-2}$  in the analysis. Also, due to contamination from the surrounding compact nebula, a simple background subtraction with an annuli region may lead to inaccurate pile-up estimate. Hence, we fit the source spectrum with a two-powerlaw model: one for the background and the other one for the pulsar. The former is fixed at the best-fit spectrum of region 12 (see Fig. 6) and we scale its amplitude according to the spatial modeling in §3.1. We found that the compact nebula provides  $0.05 \text{ cts s}^{-1}$  (1–8 keV range) to the extraction aperture and this is fixed as the nebular background in the fits. This spectral model provides an adequate fit to the 2000 data and yields a spectral index  $\Gamma = 1.1 \pm 0.1$  and an unabsorbed flux of  $6.1 \times 10^{-12} \text{ ergs cm}^{-2} \text{ s}^{-1}$  in the 0.5–10 keV range. The nebular background contributes  $\sim 20\%$  of the observed flux and the overall spectrum has a pile-up fraction less than 10%.

For the 2006 observation, we started with the same two-powerlaw model, but found that the pulsar spectrum is very close to that of the surrounding compact nebula. Therefore in the final fit, only a single absorbed powerlaw model was used. Table 3 lists the best-fit spectral parameters, indicating a much softer spectrum ( $\Gamma = 1.86 \pm 0.02$ ), with a factor of 6 increase in the unabsorbed flux ( $3.4 \times 10^{-11} \text{ ergs cm}^{-2} \text{ s}^{-1}$ ) in the second epoch. Due to spectral softening, the observed flux only changes by a factor of 4, suggesting a 6% nebular contamination and a 20% pile-up fraction despite a shorter frame time. Comparing the individual spectrum in the 2006 observation shows no short-term flux or spectral variation for the pulsar at this time. As a check for consistency, we convert the above results to the un-piled count rates for the pulsar plus the nebular background. The inferred count rates in the 1–8 keV band are 0.17 and 0.77  $\text{cts s}^{-1}$  for the 2000 and 2006 observations respectively. This is in good agreement with the independent estimate from the readout trails in the previous section. We also note that our results are mostly consistent with the values re-

ported by Kumar & Safi-Harb (2008) and Gavril et al. (2008), but the pulsar spectral index for the first epoch is slightly lower than the value reported by Helfand et al. (2003). The difference is probably the result of improvements in the pile-up model.

In order to look for any thermal emission from the neutron star, we have tried adding a blackbody component to the fits. As shown in Table 3, the PL+BB model provides a better fit to the 2006 data in terms of the reduced  $\chi^2$  value. Moreover, an  $F$ -test indicates that this model is statistically better than a single powerlaw at a 99.97% confidence level. Hence, we concluded that the thermal component is significant. The best-fit blackbody has a temperature of  $0.9 \pm 0.2$  keV and a flux  $\sim 10\%$  of the non-thermal emission. This implies a blackbody radius of  $R^\infty = 0.4 \pm 0.2$  km at 6 kpc. For the first epoch, a thermal component is not observed and we place a detection limit  $4 \times 10^{-13}$  ergs s $^{-1}$  cm $^{-2}$  at 90% confidence level in 0.5-10 keV energy range.

## 6. DISCUSSION

### 6.1. THE ENVIRONMENT AND STRUCTURE OF THE PWN

At a distance of 6 kpc, the overall PWN has a radius  $R_{\text{PWN}} \approx 20'' = 0.6$  pc and an X-ray luminosity  $L_X^{0.5-10} = 1.4 \times 10^{35}$  ergs s $^{-1}$  in the 0.5-10 keV band. A very rough estimate on the nebula magnetic field can be made based on the X-ray luminosity with the equipartition assumption, or from the SNR evolution assuming a constant pulsar spin-down power (Seward et al. 1984). They both suggest a field strength  $B \sim 40 \mu\text{G}$ . On the other hand, comparing the PWN X-ray and radio spectra (Helfand et al. 2003; Bock & Gaensler 2005) indicate a spectral break at  $\nu_b \approx 5 \times 10^{14}$  Hz (Morton et al. 2007). If this is solely due to synchrotron cooling, then the pulsar spin-down of  $\sim 800$  yr implies a nebula field of  $B \sim 100$  mG. As Morton et al. (2007) point out, this is likely to be too large for the PWN. Bock & Gaensler (2005) also suggest that the simple standard synchrotron cooling scenario may not hold for this object. Indeed there are many intrinsic and evolutionary effects that could complicate the picture (e.g., Reynolds & Chevalier 1984; Slane et al. 2008).

The HESS detection of VHE  $\gamma$ -rays from Kes 75 provides a better handle on the magnetic field (Djannati-Ataï et al. 2007). In a one zone model assuming all the TeV photons come from inverse Compton scattering with the cosmic microwave background (CMB), the X-ray and  $\gamma$ -ray fluxes are related to the energy densities of the magnetic field ( $\epsilon_B$ ) and the photons ( $\epsilon_{\text{ph}}$ ) by  $L_X/L_\gamma = \epsilon_B/\epsilon_{\text{ph}}$  where  $\epsilon_{\text{ph}} = 3.8 \times 10^{-13}$  ergs cm $^{-3}$  for the CMB. Comparing our result of X-ray flux in 0.5-10 keV band to the reported HESS detection of TeV flux in 0.3-5 TeV range suggests  $L_X/L_\gamma \sim 30$ , which is comparable to that of G21.5-0.9, implying a low magnetic field of  $B \approx 15 \mu\text{G}$  (Djannati-Ataï et al. 2007). The picture is further supported by the similar radio and X-ray PWN sizes. As compared to the radio images from the VLA and the BIMA array, the X-ray synchrotron emission extends nearly to the edge of the radio counterpart (Helfand et al. 2003; Bock & Gaensler 2005). This suggests a long synchrotron cooling time scale and hence a weak magnetic field. A nebula field  $B = 15 B_{15\mu\text{G}}$  is

adopted throughout the discussion.<sup>7</sup> This field strength gives a magnetic pressure  $10^{-11} B_{15}^2$  dyne cm $^{-2}$  in the PWN, with a magnetic energy  $2 \times 10^{44} B_{15}^2$  ergs assuming the nebular geometry is a sphere. This is only 0.1% of the total spin-down energy if the pulsar was born with a spin period close to the current value; if the pulsar's initial spin period is shorter, the fraction will be even smaller.

Numerous theoretical and numerical studies of PWN evolution within an expanding SNR suggest that during the first  $\sim 1000$  years, a PWN expands freely into the surrounding ejecta before the supernova reverse shock is reached (e.g. van der Swaluw et al. 2001; Bucciantini et al. 2003; van der Swaluw 2003; Chevalier 2005). Given the young age of Kes 75, the PWN is likely to be in the free expansion phase. The expansion of light pulsar wind materials into the dense supernova ejecta could result in Rayleigh-Taylor instabilities. This may be associated to the protrusions in the PWN boundary, similar to the optical filaments of the Crab Nebula (Hester et al. 1996). Alternatively, the protrusions in the north could also due to ordered magnetic fields, as Seward et al. (2006) proposed for the Crab PWN. Although a comparison to optical observations will help to identify the nature of these structures, this may not be observationally feasible due to the large distance of the source and its location on the Galactic plane.

To interpret the arc-like feature in the northeast, we first note that it is unlikely to be reconciled as a bow shock. Due to the young age of the system, the pulsar is not expected to move supersonically within the SNR interior. Therefore we suggest that the arc could be a toroidal termination shock, which is a commonly observed feature among young PWNe. The shock radius  $r_s$  is determined by the balance between the pulsar ram pressure and the ambient pressure  $P$ :

$$r_s^2 = \frac{\dot{E}}{4\pi c \xi P},$$

where  $\dot{E}$  is the pulsar spin-down luminosity and  $0 < \xi < 1$  is the fraction of a sphere covered by the pulsar wind (e.g.  $\xi = 2/3$  if the wind has a latitude dependence of  $\sin^2 \theta$ ). In this picture, the inferred pressure for our PWN is  $P \sim 10^{-11} \xi^{-1}$  dyne cm $^{-2}$ , consistent with the magnetic pressure inside the nebula. This is also in a general agreement with the numerical simulations of a generic young PWN evolving in a SNR (van der Swaluw et al. 2001; Bucciantini et al. 2003). Comparing to the thermal pressure in the SNR limbs (Morton et al. 2007), this value is  $\sim 100$  times lower, confirming that the supernova reverse shock has not yet reached the PWN and that most of the ejecta in the SNR interior are still cold.

In general, we do not expect any significant synchrotron emission inside the termination shock. In this case, the compact nebula surrounding the pulsar could be a result of particle injection from previous outbursts. The synchrotron cooling timescale for a particle emitting at  $\varepsilon = 5$  keV in the nebula is

$$t_{\text{synch}} = 39 B^{-3/2} \varepsilon^{-1/2} \text{ kyr} \simeq 300 B_{15}^{-3/2} \text{ yr}.$$

If an outburst occurs every decade, as suggested by Gavril et al. (2008), then based on the timescale, this

<sup>7</sup> We note that values between 10-40  $\mu\text{G}$  do not change our conclusions qualitatively.

could possibly power the emission of the compact nebula.

As an alternative, one could identify the compact nebula as a termination shock. The smaller radius  $r_s = 3.5''$  only requires a slightly larger magnetic field in the nebula and the ambient pressure is still much lower than the thermal pressure in the rims. In this scenario, the arc-like feature could be interpreted as an analogue to the outer arc in G320.4–1.2 powered by PSR B1509–58, which Gaensler et al. (2002) argue is a wisp in the equatorial outflow based on the particles flowing timescale. In our case, the flowing timescale from the compact nebula to the arc-like feature is

$$t_{\text{flow}} = \frac{3r_s}{c} \left( \frac{r}{r_s} \right)^3 = 30 \left( \frac{r_s}{3.5''} \right)^{-2} \left( \frac{r}{10.1''} \right)^3 \text{ yr},$$

which is shorter than  $t_{\text{synch}}$ . This indicates a different physical origin of the arc than the Crab Nebula's bright outer torus, where most X-ray emitting particles lose their energy. In contrast to the Crab Nebula's wisp (Hester et al. 2002), our data do not indicate any significant proper motion in the arc. Similar results have also been reported for the arc surrounding PSR B1509–58 (DeLaney et al. 2006), and the radio wisp in 3C 58 (Bietenholz 2006). If the variability in our case is compatible, it would be below the current detection sensitivity given the relatively shallow exposure of the first epoch.

Finally, we discuss the spectral softening of the PWN with increasing distance from the pulsar, as shown in Fig. 7. This is a result of particle energy dissipation due to synchrotron burn-off and nebula expansion. Although some theoretical models predict a rapid increase in the spectral index (e.g., fig. 4 in Slane et al. 2004), such degree of variation is not observed here. Indeed the variation  $\Delta\Gamma = 0.5$  in our case is smaller than many other systems, such as 3C 58 or G21.5–0.9 (Slane et al. 2000, 2004), indicating a long synchrotron cooling time in the PWN. The slightly softer spectrum in the innermost bin could be due to the injection of lower energy particles from any pulsar bursts in the past, or simply because the next two bins are contaminated by the polar outflow which has a harder spectrum.

## 6.2. THE POLAR OUTFLOW

The jet-like features along the PWN symmetric axis show systematically harder spectra than their surroundings, indicating a large velocity in the polar outflow, i.e.  $t_{\text{synch}} > t_{\text{flow}}$ . If the absence of a counter inner jet in the north is due to Doppler boosting, then its detection limit provides an estimate of the flow speed. The flux ratio between the inner jet and its expected counterpart is given by

$$\frac{f_j}{f_{cj}} = \left( \frac{c + v_j \cos \zeta}{c - v_j \cos \zeta} \right)^{1+\Gamma}$$

(Pelling et al. 1987). From the the best-fit inclination angle  $\zeta = 62^\circ$  and the photon index  $\Gamma = 1.7$  for the jet, the detection limit on the counter jet sets its minimum bulk velocity  $v_j > 0.4c$ . This is comparable to jets in other pulsars such as the Crab, Vela and B1509–58 (Hester et al. 2002; Pavlov et al. 2003; Gaensler et al. 2002). To estimate the magnetic field in the jet, we approximate the southern inner jet by a cylinder with  $1.5''$  diameter

and a length of  $l_j = 3.5''$ , which correspond to 0.04 and 0.1 pc respectively at 6 kpc. The best-fit spectral luminosity  $L_{5 \text{ keV}} = 1.5 \times 10^{31} \text{ ergs s}^{-1} \text{ keV}^{-1}$  at 5 keV suggests an equipartition field  $B_j \sim 120(1 + \mu)^{2/7} \phi^{-2/7} \mu\text{G}$  with a total energy  $E_j \sim 5(1 + \mu)^{4/7} \phi^{3/7} \times 10^{43} \text{ ergs}$  for the inner jet, where  $\mu$  is the ion to electron energy and  $0 < \phi < 1$  is the filling factor (see Gaensler et al. 2002). The synchrotron cooling time for particles emitting at 5 keV in the jet is then  $t_{\text{synch}} = 13 \text{ yr}$ , confirming that  $t_{\text{synch}} \gg t_{\text{flow}} \sim l_j/v_j = 0.8 \text{ yr}$ . This also implies a minimum power input from the pulsar  $\dot{E}_j \sim E_j/t_{\text{synch}} = 1.2 \times 10^{35} \text{ ergs s}^{-1}$ , which is 1.4% of the total spin-down luminosity.

We argue that the variability in the polar outflow is unlikely due to the recent pulsar bursts. Since the 2006 observation was carried out 7 days after the bursts, materials traveling from the pulsar to the end of the inner jet requires an apparent superluminal motion  $v_{\text{app}} \approx 20c$  in the plane of the sky, which is related to the true space velocity  $\beta$  by  $v_{\text{app}} = \frac{\beta \sin \theta}{1 - \beta \cos \theta}$ , where  $\theta$  is the angle between the direction of motion and the observer line of sight. As  $\beta \leq 1$ , this places an upper limit  $\theta \leq 5.7^\circ$ . The best-fit pulsar spin axis inclination  $\zeta = 62^\circ \gg 5.7^\circ$  indicates that the observed variability in the jet could not be explained by any superluminal motion in the polar outflow. For any emission in a random direction that beamed towards the Earth with  $\theta \leq 5.7^\circ$ , there is an additional constraint for the alignment with the jet direction on the plane of the sky. Therefore the chance probability is very small and we conclude that the variability of the inner jet is almost certainly unrelated to the recent bursts.<sup>8</sup> A similar argument also applies to the northern clump. Due to the strong magnetic field and compact size of the inner jet, the Alfvén crossing time is in the order of 100 days, which is comparable to  $t_{\text{flow}}$ . Given the two epochs separate by 6 years, we could not distinguish whether the inner jet variability is due to MHD instability as is possibly so in the cases of Vela and PSR B1509–58 jets (Pavlov et al. 2003; DeLaney et al. 2006), or simply due to materials flowing downstream.

As one moves downstream along the jet, spectral softening is generally expected as a result of synchrotron burn-off. However, the outer jet region shows some hints of a harder spectrum than the inner jet, which is difficult to understand unless there is a continuous particle acceleration along the way (Hjellming & Johnston 1988) or particle injection from a shock (see below). An alternative explanation could be variability in the absorption column density, although this requires a nearly 20% change in  $N_{\text{H}}$  across the regions (Table 4). Further out along the jet direction, emission on both sides of the pulsar terminates abruptly at the northern and southern clumps. The similar spectral indices of the two clumps hint that the emission may come from the same physical process, but their relative brightness suggests that they could not be simply reconciled as Doppler boosted jets. It is possible that the clumps are results of non-thermal emission from the shock interaction between the polar outflow and the ambient medium. When the supersonic

<sup>8</sup> However, this does not completely rule out the possibility that the variability is due to any previous bursts which occurred years ago.

pulsar jets encounter the supernova ejecta, the density gradient results in a bow shock and leads to strong X-ray emission. Indeed the sharp edge of the PWN near the southern clump provides some evidence of such a density gradient and this likely results in the clump. The one in the north is less obvious, which could be due to projection effects. Comparing to other PWN systems, a similar scenario has been proposed to associate the X-ray features in RCW 89 with PSR B1509–58 (Tamura et al. 1996; Yatsu et al. 2005). The difference in our case is that the clumps are found on both sides and much closer to the pulsar. Besides, the clumps are likely to be non-thermal. Also, due to the younger age of Kes 75, the jets would encounter a cold ambient medium which has not yet been heated up by the supernova reverse shock. If we compare to other astrophysical jets (e.g. Harris & Krawczynski 2006; de Gouveia dal Pino 2005), the clumps may be identified as analogues to the terminal hotspots in the extragalactic jets, which usually have non-thermal spectra well-modeled by synchrotron or synchrotron self-Compton emission (Harris 2001). Then the outer jet in our case could be a backflow cocoon formed by the postshock materials, and the hard spectrum in the region could be related to the shock accelerated particles. Moreover, the variability of the northern clump can be attributed to Rayleigh-Taylor instabilities, as the jet expands into the much denser ejecta. The luminosity of the northern clump is  $1.2 \times 10^{34} \text{ erg s}^{-1} = 0.1 \dot{E}_j$ , which can be easily powered by the jets, and the flow time scale  $R_{\text{PWN}}/v_j < 20''/0.4c = 5 \text{ yr}$  is substantially shorter than the synchrotron cooling time  $t_{\text{synch}} = 13 \text{ yr}$ . Therefore the particles are still energetic on reaching the edge of the PWN. Future multi-wavelength observations, in particular high resolution radio maps of the PWN could help to further investigate the nature of the clumps.

### 6.3. THE NEUTRON STAR

The best-fit pulsar spectrum for the second epoch indicates a  $\sim 10\%$  flux contribution from the blackbody component, which is not observed in the 2000 data. This suggests that the thermal emission is likely related to the afterglow of the recent bursts, and could be part of the transition between a rotation-powered pulsar to a magnetar with persistent emission as pointed out by Gavril et al. (2008). In the quiescent state, our flux measurement indicates a pulsar luminosity  $L_{\text{X},0.5-10}^{\text{PSR}} = 2.6 \times 10^{34} \text{ erg s}^{-1}$ . As mentioned in the introduction, the original 19 kpc distance estimate implies enormous X-ray efficiencies for the pulsar and the PWN. The new distance estimate of 6 kpc greatly reduces the pulsar luminosity by an order of magnitude. Now the pulsar has an X-ray efficiency  $\eta_{\text{PSR}} \equiv L_{\text{X}}^{\text{PSR}}/\dot{E} \approx 0.3\%$ , which is no longer an outlier, but rather typical among young neutron stars (see Kargaltsev & Pavlov 2008). For the PWN, the luminosity  $L_{\text{X},0.5-10}^{\text{PWN}} = 1.4 \times 10^{35} \text{ erg s}^{-1}$  and efficiency  $\eta_{\text{PWN}} \approx 2\%$  are still larger than many others, but not exceptional. Also,  $\eta_{\text{PWN}}/\eta_{\text{PSR}} = 6$  is close to the mean value of 4 obtained by Kargaltsev & Pavlov (2008). Our results indicate that the X-ray properties of PSR J1846–0258 in quiescence are not much different from an ordinary young neutron star’s. As compared to the Crab pulsar, PSR J1846–0258 has a higher surface magnetic field but its nebular field is much weaker. This

seems to imply no direct correlation between the magnetic field strengths on a neutron star surface and in its surrounding PWN.

Although the exact nature of the arc-like feature remains unknown, in either the equatorial torus or equatorial wisp interpretation, the pulsar spin orientation can still be inferred from the spatial modeling. Livingstone et al. (2006) propose a scenario in which the angle between the spin and magnetic axis is  $\alpha \approx 9^\circ$  in order to explain the pulsar’s braking index in terms of the vacuum-dipole model (Melatos 1997). If this is real, then the spin inclination  $\zeta = 63^\circ$  obtained from the torus fitting indicates a magnetic inclination  $\beta = \zeta - \alpha \approx 54^\circ$ . The large  $\beta$  is consistent with the non-detection of radio pulsations. This picture also predicts that no pulsed  $\gamma$ -rays will be observable according to the Romani & Yadigaroglu (1995) model. Future GLAST observations will address this.

### 7. CONCLUSIONS

In this study, we have carried out detailed spatial and spectral analysis of the PWN in Kes 75. The deep Chandra observations reveal the axisymmetric structure of the PWN with jet and torus features. We deduce an average nebula field  $B \sim 15 \mu\text{G}$  from the X-ray emissivity and interpret the arc-like structure in the northeast as equatorial outflow, either a toroidal termination shock or a wisp. We further apply a torus fitting scheme and show that the arc has a radius of  $10.1'' \pm 0.4''$ , inclined at  $62 \pm 2^\circ$  to the plane of the sky with the symmetry axis at a position angle  $207^\circ \pm 8^\circ$ . The spatially resolved spectrum of the PWN shows that regions along the jet direction have systematically harder spectrum than the surroundings, suggesting a high velocity in the polar outflow. We also deduce a minimum flow velocity of  $0.4c$  based on the non-detection of a counter jet. There are two bright clumps aligned with the jet, which we propose due to bow shocks of the polar outflow in the supernova ejecta. Over a period of 6 years, the northern clump and the inner jet demonstrate strong variability, which could be attributed to MHD instabilities. Accompanying the recent outburst, the pulsar luminosity has increased by 6 times and shows substantial softening in the spectrum. We also find an emerging thermal component in the pulsar spectrum, which could be related to the thermal afterglow of the bursts. The 2000 observation suggests a pulsar X-ray efficiency of 0.3%. This value is not particularly large among young neutron stars. In this aspect, PSR J1846–0258 was a rather typical pulsar in X-rays during quiescence.

Further investigation of the PWN properties will require high resolution multi-wavelength observations. Also, long-term monitoring of the source would be fruitful. The evolution of the thermal component in the pulsar spectrum can indicate any physical changes of the hotspot on the neutron star surface, thus probing the nature of the bursts. Moreover, as this is the only known example of magnetar-like bursts inside a PWN, any flux variation in the nebula that is associated with the bursts could reveal the energy transport in the system. This connection provides a unique opportunity to improve our understanding of both PWN and magnetar physics.

We thank Mallory Roberts for useful discussions. P.O.S. acknowledges support from NASA contract

NAS8-39073 and Chandra Grant G06-7053X. B.M.G. acknowledges the support of an Australian Research Coun-

cil Federation Fellowship.  
*Facilities:* CXO (ACIS)

#### REFERENCES

- Archibald, A. M., Kaspi, V. M., Livingstone, M. A., & McLaughlin, M. A. 2008, *ApJ*, submitted, arXiv:0805.1448
- Becker, R. H., & Helfand, D. J. 1984, *ApJ*, 283, 154
- Bietenholz, M. F. 2006, *ApJ*, 645, 1180
- Bietenholz, M. F., & Bartel, N. 2008, *MNRAS*, 386, 1411
- Blanton, E. L., & Helfand, D. J. 1996, *ApJ*, 470, 961
- Bock, D. C.-J., & Gaensler, B. M. 2005, *ApJ*, 626, 343
- Bucciantini, N., Blondin, J. M., Del Zanna, L., & Amato, E. 2003, *A&A*, 405, 617
- Chevalier, R. A. 2005, *ApJ*, 619, 839
- Davis, J. E. 2001, *ApJ*, 562, 575
- de Gouveia dal Pino, E. M. 2005, *Advances in Space Research*, 35, 908
- DeLaney, T., Gaensler, B. M., Arons, J., & Pivovarov, M. J. 2006, *ApJ*, 640, 929
- Del Zanna, L., Volpi, D., Amato, E., & Bucciantini, N. 2006, *A&A*, 453, 621
- Djannati-Ataï, A., De Jager, O. C., Terrier, R., Gallant, Y. A., & Hoppe, S. for the H.E.S.S. Collaboration, 2007, in *Proceedings of the 30th ICRC (Merida, Mexico)*, in press, (arXiv:0710.2247)
- Gaensler, B. M., Arons, J., Kaspi, V. M., Pivovarov, M. J., Kawai, N., & Tamura, K. 2002, *ApJ*, 569, 878
- Gaensler, B. M., & Slane, P. O. 2006, *ARA&A*, 44, 17
- Gavril, F. P., Gonzalez, M. E., Gotthelf, E. V., Kaspi, V. M., Livingstone, M. A., 2008, *Science*, 319, 1802
- Gotthelf, E. V., Vasisht, G., Boylan-Kolchin, M., & Torii, K. 2000, *ApJ*, 542, L37
- Harris, D. E. 2001, in *ASP Conf. Ser. 250, Particles and Fields in Radio Galaxies Conference*, ed. R. A. Laing & K. M. Blundell, (San Francisco: ASP), 204
- Harris, D. E., & Krawczynski, H. 2006, *ARA&A*, 44, 463
- Helfand, D. J., Collins, B. F., & Gotthelf, E. V. 2003, *ApJ*, 582, 783
- Hester, J. J., et al. 1996, *ApJ*, 456, 225
- Hester, J. J., et al. 2002, *ApJ*, 577, L49
- Hjellming, R. M., & Johnston, K. J. 1988, *ApJ*, 328, 600
- Kargaltsev, O., & Pavlov, G. G. 2008, in *AIP Conf. Proc. 983, 40 Years of Pulsars: Millisecond Pulsars, Magnetars and More*, ed. C. Bassa, Z. Wang, A. Cumming, & V.M. Kaspi, (New York: AIP), 171
- Kesteven, M. J. L. 1968, *Australian Journal of Physics*, 21, 369
- Leahy, D. A., & Tian, W. 2008, *A&A*, 480, 25
- Livingstone, M. A., Kaspi, V. M., Gotthelf, E. V., & Kuiper, L. 2006, *ApJ*, 647, 1286
- Melatos, A. 1997, *MNRAS*, 288, 1049
- McBride, V. A., et al. 2008, *A&A*, 477, 249
- Morton, T. D., Slane, P., Borkowski, K. J., Reynolds, S. P., Helfand, D. J., Gaensler, B. M., & Hughes, J. P. 2007, *ApJ*, 667, 219
- Mori, K., Burrows, D. N., Hester, J. J., Pavlov, G. G., Shibata, S., & Tsunemi, H. 2004, *ApJ*, 609, 186
- Ng, C.-Y., & Romani, R.W. 2008, *ApJ*, 673, 411
- Pavlov, G. G., Teter, M. A., Kargaltsev, O., & Sanwal, D. 2003, *ApJ*, 591, 1157
- Pelling, R. M., Paciesas, W. S., Peterson, L. E., Makishima, K., Oda, M., Ogawara, Y., & Miyamoto, S. 1987, *ApJ*, 319, 416
- Reynolds, S. P., & Chevalier, R. A. 1984, *ApJ*, 278, 630
- Romani, R. W., & Yadigaroglu, I.-A. 1995, *ApJ*, 438, 314
- Sanjeev Kumar, H., & Safi-Harb, S. 2008, *ApJ*, in press, (arXiv:0802.1242)
- Seward, F. D., Harnden, F. R., Jr., Szymkowiak, A., & Swank, J. 1984, *ApJ*, 281, 650
- Seward, F. D., Tucker, W. H., & Fesen, R. A. 2006, *ApJ*, 652, 1277
- Slane, P., Chen, Y., Schulz, N. S., Seward, F. D., Hughes, J. P., & Gaensler, B. M. 2000, *ApJ*, 533, L29
- Slane, P., Helfand, D. J., Reynolds, S. P., Gaensler, B. M., Lemiére, A., & Wang, Z. 2008, *ApJ*, 676, 33
- Slane, P., Helfand, D. J., van der Swaluw, E., & Murray, S. S. 2004, *ApJ*, 616, 403
- Tamura, K., Kawai, N., Yoshida, A., & Brinkmann, W. 1996, *PASJ*, 48, L33
- van der Swaluw, E. 2003, *A&A*, 404, 939
- van der Swaluw, E., Achterberg, A., Gallant, Y. A., & Tóth, G. 2001, *A&A*, 380, 309
- Warwick, R. S., et al. 2001, *A&A*, 365, L248
- Woods, P. M., & Thompson, C. 2006, in *Compact stellar X-ray sources*, ed. W. H. G. Lewin & M. van der Klis (Cambridge: Cambridge Univ. Press), 547
- Yatsu, Y., Kawai, N., Kataoka, J., Kotani, T., Tamura, K., & Brinkmann, W. 2005, *ApJ*, 631, 312



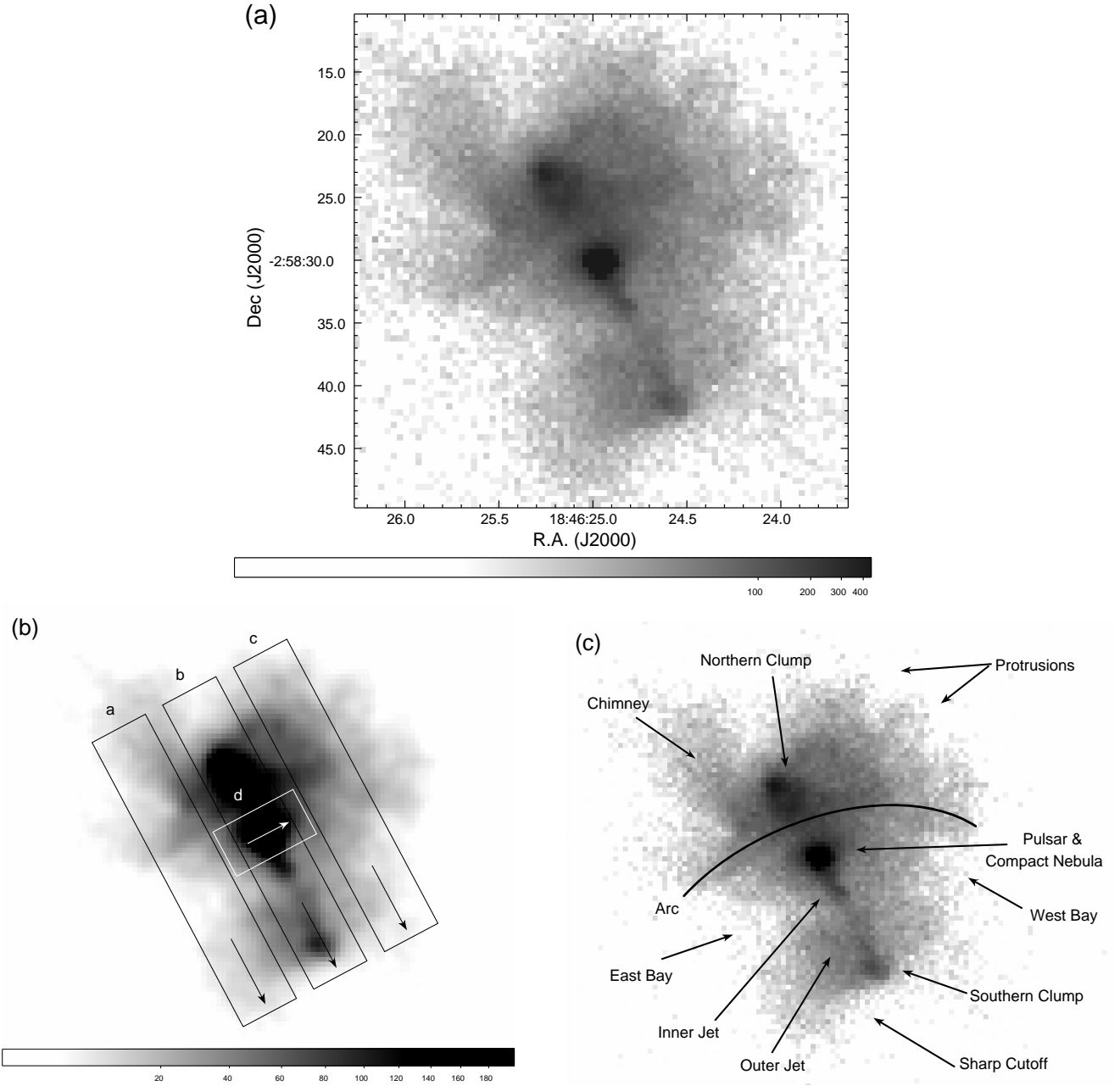


FIG. 1.— (a) A Chandra ACIS-S image of the PWN in Kes 75 in the 1-8 keV energy range from the 2006 observation. (b) The same image lightly smoothed with 1'' FWHM Gaussian, and shown in a different stretch to emphasize the faint structure. The boxes show the extraction regions for the count profiles in Fig 2, with the arrows indicating the positive  $x$  direction in the plots. (c) Small-scale features in the PWN.

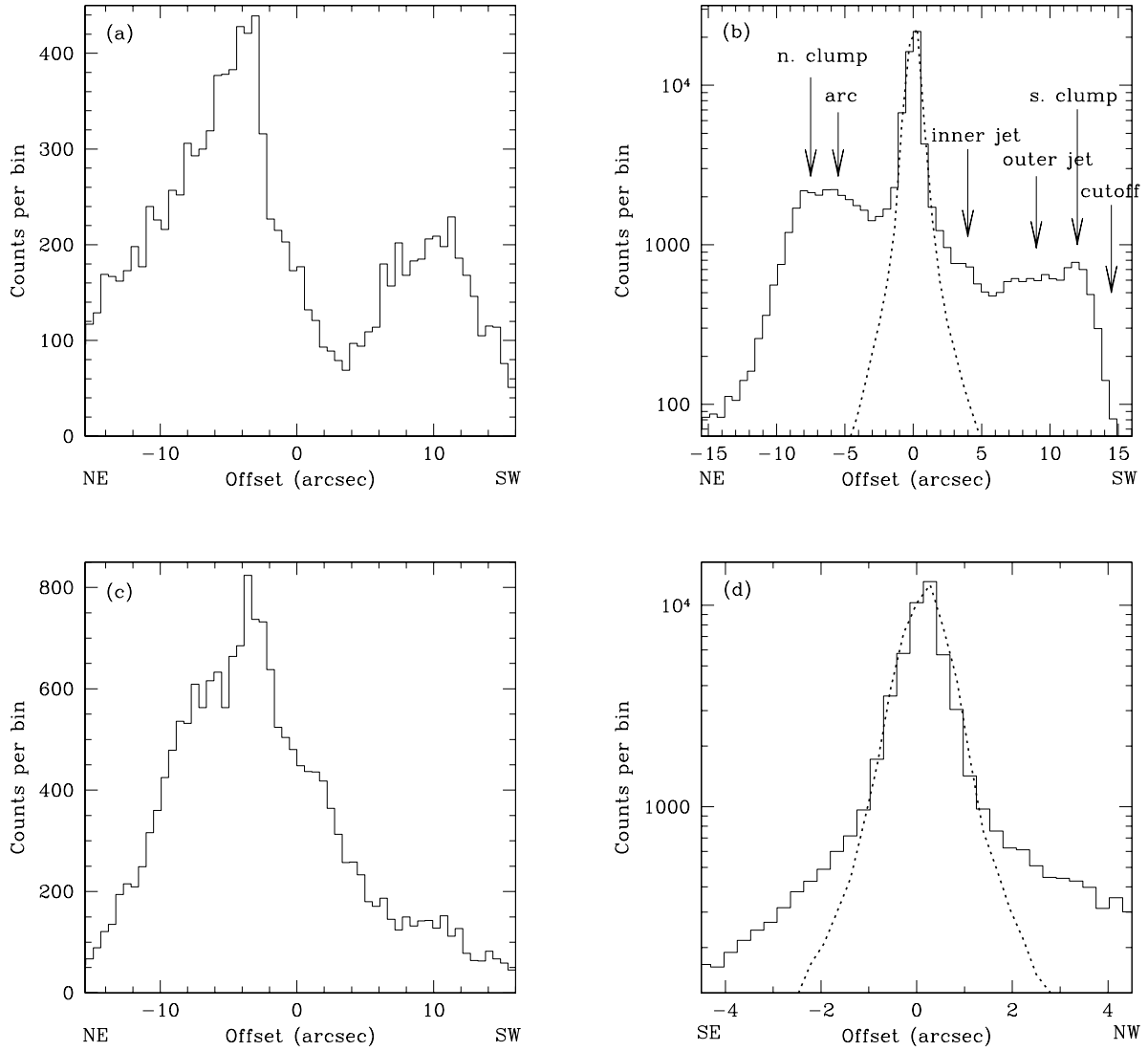


FIG. 2.— Count profiles along different regions pulsar in Fig. 1, extracted from the 2006 data in 1-8 keV energy range. The  $x$ -axis is the offset from the pulsar position, in arcseconds. The solid and dotted lines corresponding to the data and the model PSF respectively. The latter is generated using the source spectrum with CCD pile-up effects included. Panel (b) illustrates the features along the nebula symmetry axis, while panel (d) shows the compact diffuse emission surrounding the pulsar. The peaks in panels (a) & (c) clearly illustrate the arc-like feature in the north.

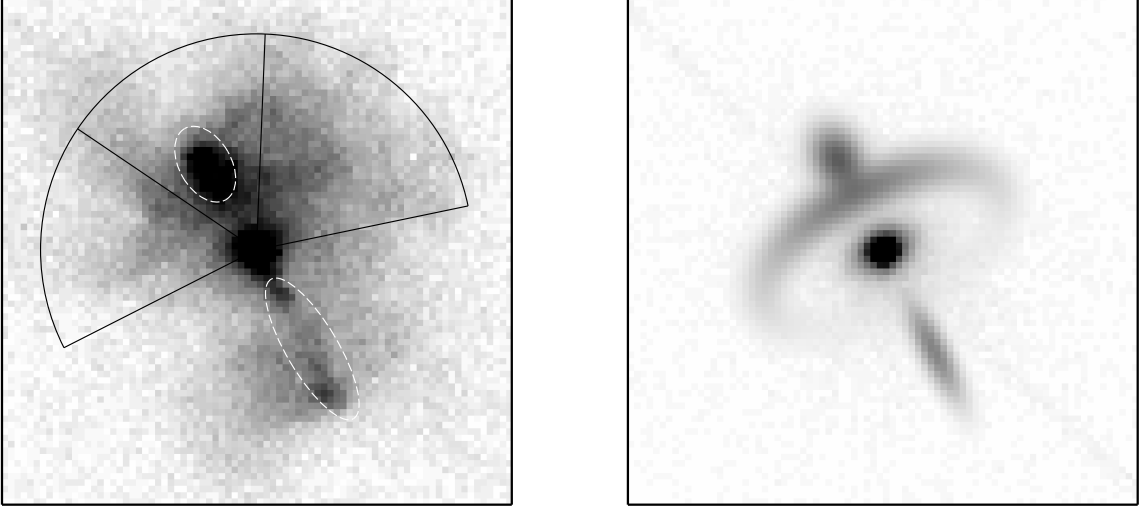


FIG. 3.— *Left*: same as Fig. 1a, showing the regions excised for systematic errors estimate in the torus fitting (see text). *Right*: best-fit torus+jet model to the PWN structure.

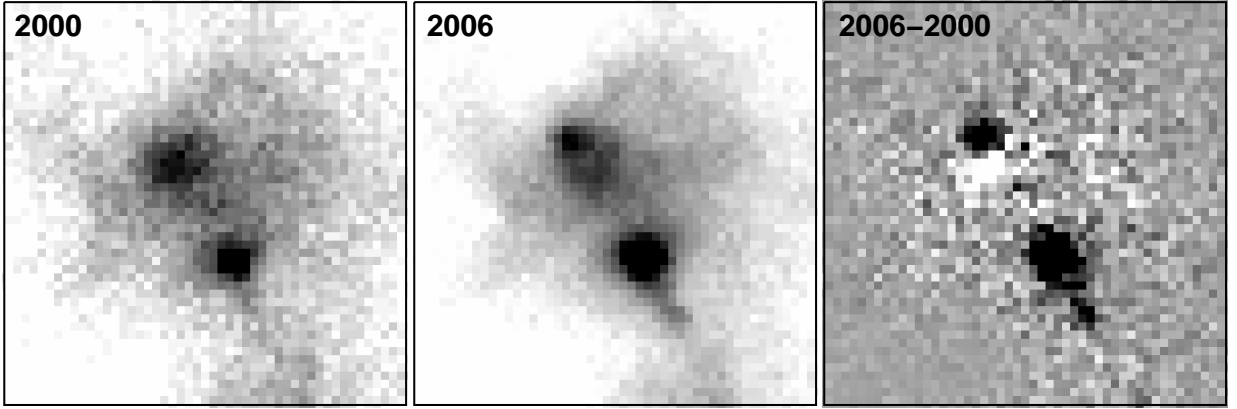


FIG. 4.— Exposure corrected images of the PWN in Kes 75 in the 1-8 keV band, generated with weighted exposure maps using the best-fit PWN spectrum. The first and second epoch are shown in the left and middle panels respectively with log scales ranging from 0 to  $10^{-4}$   $\text{cts cm}^{-2} \text{s}^{-1} \text{pixel}^{-1}$ . The right panel shows the difference when the 2000 image is subtracted from the 2006 image. This greyscale is linear, ranging from  $-10^{-6}$  to  $10^{-6}$   $\text{cts cm}^{-2} \text{s}^{-1} \text{pixel}^{-1}$ .

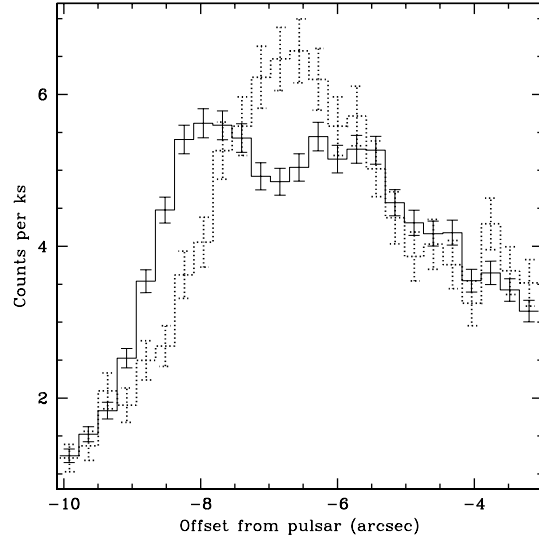


FIG. 5.— Count profiles of the northern clump in the PWN of Kes 75, extracted in a  $4''$  wide rectangular region along the jet direction in the 1–8 keV range. The first and second epochs are shown by the dotted and solid lines respectively.

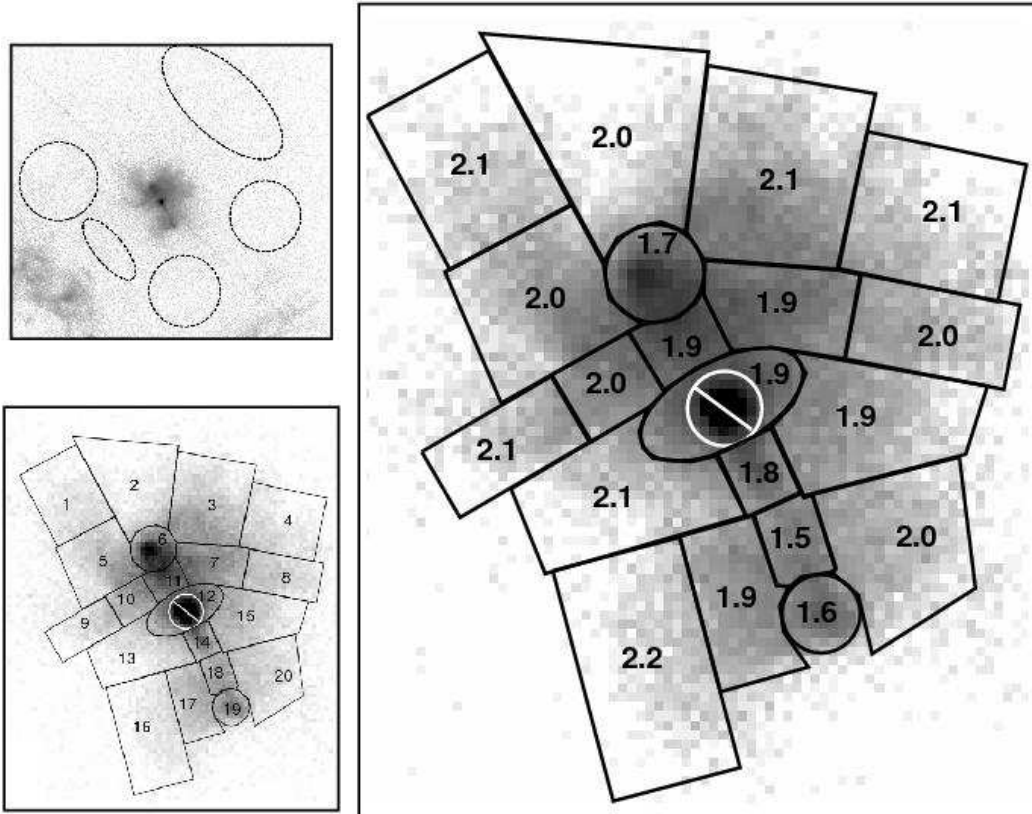


FIG. 6.— *Top left*: background regions used in the overall PWN and pulsar spectral analysis. *Bottom left*: extraction regions for the PWN spectrum. *Right*: best-fit powerlaw indices for the 2006 observation.

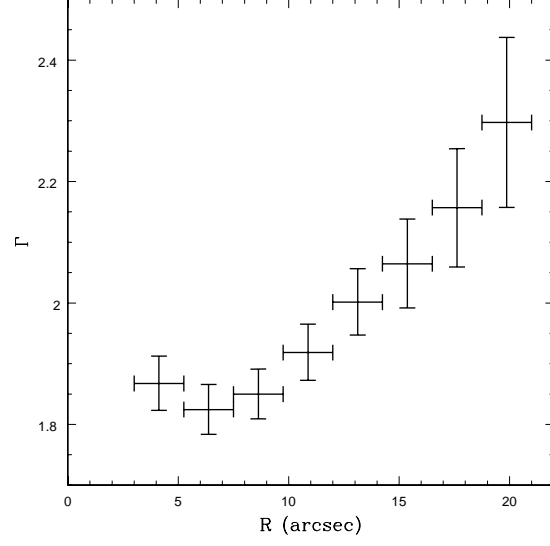


FIG. 7.— Variation of the PWN photon index in Kes 75 with the radius from the central pulsar.

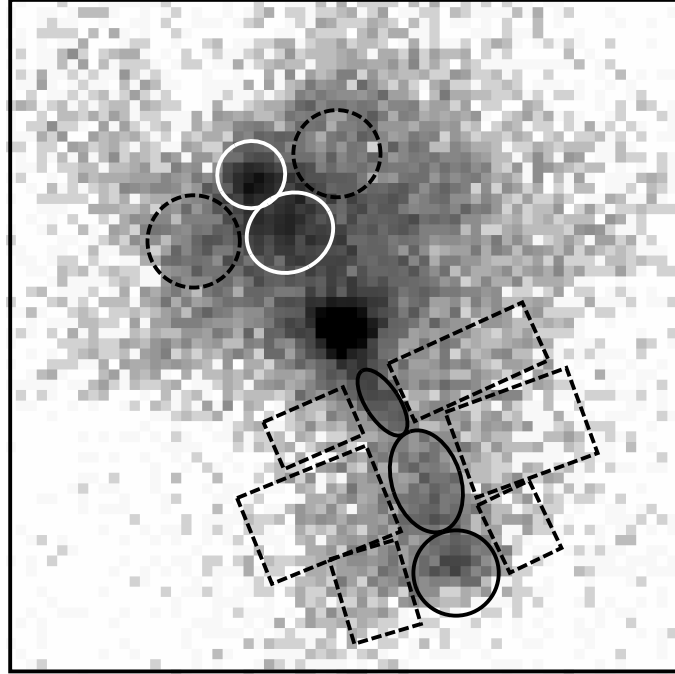


FIG. 8.— Extraction regions for the PWN features shown by the solid regions from north to south: northern clump 1, northern clump 2, inner jet, outer jet, southern clump. The corresponding backgrounds are extracted from the adjacent regions shown by the dotted lines. The underlying image is the 2006 data in the 5-9 keV energy band, showing high energy emission in the PWN.

TABLE 1  
BEST-FIT TORUS PARAMETERS.

Parameter	Value
$\Psi$	$207^\circ \pm 8^\circ$
$\zeta$	$62^\circ \pm 5^\circ$
$R$	$10'' \pm 1''$
blur	$1''$ (fixed)
$\beta$	$0.76 \pm 0.05$
Point Source	$61.6 \times 10^3$ cts
Torus	$26.2 \times 10^3$ cts
Compact Nebula	$9.1 \times 10^3$ cts
Northern Jet	$12.2 \times 10^3$ cts
Southern Jet	$6.4 \times 10^3$ cts

TABLE 2  
SPECTRAL FITS TO THE PWN.

	$\Gamma$	$f_{0.5-10}^{\text{abs}}$	$\Gamma$	$f_{0.5-10}^{\text{abs}}$	$\Gamma$	$f_{0.5-10}^{\text{abs}}$	$\Gamma$	$f_{0.5-10}^{\text{abs}}$
	2000				2006			
$N_H$	$3.9 \pm 0.1$		$4.0$ (fixed)		$4.06 \pm 0.07$		$4.0$ (fixed)	
region 1	$2.3 \pm 0.3$	$2.1 \pm 0.2$	$2.3 \pm 0.3$	$2.1 \pm 0.2$	$2.10 \pm 0.13$	$2.7 \pm 0.1$	$2.07 \pm 0.12$	$2.7 \pm 0.1$
region 2	$2.1 \pm 0.3$	$2.9 \pm 0.2$	$2.2 \pm 0.2$	$2.9 \pm 0.2$	$2.05 \pm 0.11$	$3.5 \pm 0.1$	$2.02 \pm 0.10$	$3.5 \pm 0.1$
region 3	$2.0 \pm 0.1$	$12.9 \pm 0.5$	$2.1 \pm 0.1$	$12.8 \pm 0.5$	$2.06 \pm 0.06$	$13.6 \pm 0.2$	$2.04 \pm 0.05$	$13.7 \pm 0.2$
region 4	$1.7 \pm 0.2$	$3.4 \pm 0.3$	$1.8 \pm 0.2$	$3.4 \pm 0.3$	$2.09 \pm 0.11$	$3.5 \pm 0.1$	$2.07 \pm 0.10$	$3.5 \pm 0.1$
region 5	$1.9 \pm 0.1$	$9.9 \pm 0.4$	$2.0 \pm 0.1$	$9.9 \pm 0.4$	$2.01 \pm 0.07$	$9.4 \pm 0.2$	$1.99 \pm 0.06$	$9.4 \pm 0.2$
region 6	$1.8 \pm 0.1$	$19.5 \pm 0.6$	$1.8 \pm 0.1$	$19.4 \pm 0.6$	$1.75 \pm 0.05$	$21.1 \pm 0.3$	$1.73 \pm 0.04$	$21.2 \pm 0.3$
region 7	$1.9 \pm 0.1$	$16.7 \pm 0.5$	$2.0 \pm 0.1$	$16.6 \pm 0.5$	$1.94 \pm 0.05$	$15.9 \pm 0.3$	$1.91 \pm 0.04$	$16.0 \pm 0.3$
region 8	$1.7 \pm 0.2$	$4.6 \pm 0.3$	$1.7 \pm 0.2$	$4.6 \pm 0.3$	$1.99 \pm 0.10$	$4.3 \pm 0.1$	$1.97 \pm 0.09$	$4.3 \pm 0.1$
region 9	$2.4 \pm 0.3$	$1.5 \pm 0.2$	$2.4 \pm 0.3$	$1.5 \pm 0.2$	$2.08 \pm 0.15$	$2.1 \pm 0.1$	$2.05 \pm 0.14$	$2.1 \pm 0.1$
region 10	$1.8 \pm 0.2$	$6.7 \pm 0.4$	$1.8 \pm 0.2$	$6.6 \pm 0.4$	$1.99 \pm 0.08$	$6.0 \pm 0.2$	$1.96 \pm 0.08$	$6.0 \pm 0.2$
region 11	$1.8 \pm 0.1$	$12.6 \pm 0.5$	$1.8 \pm 0.1$	$12.5 \pm 0.5$	$1.83 \pm 0.06$	$12.3 \pm 0.2$	$1.80 \pm 0.05$	$12.4 \pm 0.2$
region 12	$1.9 \pm 0.1$	$10.8 \pm 0.4$	$1.9 \pm 0.1$	$10.7 \pm 0.4$	$1.91 \pm 0.06$	$12.0 \pm 0.2$	$1.88 \pm 0.05$	$12.1 \pm 0.2$
region 13	$2.0 \pm 0.2$	$3.7 \pm 0.3$	$2.0 \pm 0.2$	$3.7 \pm 0.3$	$2.10 \pm 0.10$	$4.0 \pm 0.1$	$2.07 \pm 0.09$	$4.0 \pm 0.1$
region 14	$1.8 \pm 0.2$	$3.9 \pm 0.3$	$1.9 \pm 0.2$	$3.8 \pm 0.3$	$1.83 \pm 0.09$	$5.6 \pm 0.2$	$1.81 \pm 0.08$	$5.6 \pm 0.2$
region 15	$1.7 \pm 0.1$	$8.4 \pm 0.4$	$1.7 \pm 0.1$	$8.3 \pm 0.4$	$1.86 \pm 0.07$	$8.8 \pm 0.2$	$1.84 \pm 0.06$	$8.8 \pm 0.2$
region 16	$2.1 \pm 0.2$	$2.8 \pm 0.2$	$2.1 \pm 0.2$	$2.8 \pm 0.2$	$2.20 \pm 0.12$	$2.8 \pm 0.1$	$2.17 \pm 0.12$	$2.8 \pm 0.1$
region 17	$1.7 \pm 0.2$	$7.1 \pm 0.4$	$1.7 \pm 0.2$	$7.1 \pm 0.4$	$1.93 \pm 0.08$	$6.7 \pm 0.2$	$1.90 \pm 0.07$	$6.7 \pm 0.2$
region 18	$1.4 \pm 0.2$	$5.6 \pm 0.4$	$1.4 \pm 0.2$	$5.6 \pm 0.4$	$1.57 \pm 0.10$	$5.0 \pm 0.2$	$1.54 \pm 0.09$	$5.0 \pm 0.2$
region 19	$1.7 \pm 0.2$	$5.2 \pm 0.3$	$1.7 \pm 0.2$	$5.2 \pm 0.3$	$1.65 \pm 0.09$	$5.6 \pm 0.2$	$1.63 \pm 0.08$	$5.7 \pm 0.2$
region 20	$1.9 \pm 0.2$	$4.7 \pm 0.3$	$1.9 \pm 0.2$	$4.7 \pm 0.3$	$1.99 \pm 0.09$	$5.2 \pm 0.2$	$1.96 \pm 0.08$	$5.2 \pm 0.2$
total	$1.84 \pm 0.07$	$141 \pm 2$	$1.88 \pm 0.03$	$139 \pm 2$	$1.93 \pm 0.03$	$143 \pm 0.8$	$1.89 \pm 0.02$	$144 \pm 0.8$

NOTE. —  $N_H$  is in the unit of  $10^{22} \text{ cm}^{-2}$  and  $f_{0.5-10}^{\text{abs}}$  is the absorbed flux in the 0.5-10 keV range in the unit of  $10^{-13} \text{ ergs s}^{-1} \text{ cm}^{-2}$ . The uncertainties quoted are 90% confidence intervals.

TABLE 3  
SPECTRAL FITS TO PSR J1846-0258

Model	$N_H$	$\Gamma$	$f_{0.5-10}^{\text{abs,PL}}$	$f_{0.5-10}^{\text{unabs,PL}}$	$kT$ (keV)	$f_{0.5-10}^{\text{abs,BB}}$	$f_{0.5-10}^{\text{unabs,BB}}$	$\chi^2/\nu$
2000								
PL	$4.0^\dagger$	$1.1 \pm 0.1$	$0.42 \pm 0.02$	$0.61 \pm 0.03$	...	...	...	36.4/40
PL+BB	$4.0^\dagger$	$1.0^{+0.8}_{-0.3}$	$0.42 \pm 0.02$	$0.61 \pm 0.04$	$0.4 \pm 0.4$	$0.001^{+0.003}_{-0.001}$	$0.01^{+0.03}_{-0.01}$	35.6/38
2006								
PL	$4.0^\dagger$	$1.86 \pm 0.02$	$1.64 \pm 0.03$	$3.7 \pm 0.1$	...	...	...	148.8/136
PL+BB	$4.0^\dagger$	$1.9 \pm 0.1$	$1.3 \pm 0.3$	$3.1 \pm 0.6$	$0.9 \pm 0.2$	$0.17 \pm 0.02$	$0.32 \pm 0.04$	132.1/134

NOTE. —  $N_H$  is in the unit of  $10^{22} \text{ cm}^{-2}$ .  $f_{0.5-10}^{\text{abs,PL}}$  and  $f_{0.5-10}^{\text{unabs,PL}}$  are the absorbed and unabsorbed fluxes respectively for the powerlaw component, while  $f_{0.5-10}^{\text{abs,BB}}$  and  $f_{0.5-10}^{\text{unabs,BB}}$  are the absorbed and unabsorbed fluxes for the blackbody component. All the reported fluxes are in units of  $10^{-11} \text{ ergs s}^{-1} \text{ cm}^{-2}$  in the 0.5-10 keV range. The uncertainties quoted are 90% confidence intervals.

$^\dagger$  – held fixed in the fit.

TABLE 4  
SPECTRAL FITS TO THE JET AND CLUMP FEATURES

Region	Model	$N_H$	$\Gamma / kT$ (keV)	$f_{0.5-10}^{\text{abs}}$	$f_{0.5-10}^{\text{unabs}}$	$\chi^2/\nu$
2000						
northern clump	PL	$4.0^\dagger$	$1.6 \pm 0.1$	$15.0 \pm 0.7$	$28.2 \pm 1.4$	14/16
inner jet	PL	$4.0^\dagger$	$1.6 \pm 0.5$	$1.2 \pm 0.2$	$2.2 \pm 0.4$	6.3/9
outer jet	PL	$4.0^\dagger$	$1.1 \pm 0.3$	$4.0 \pm 0.4$	$6.0 \pm 0.6$	5.5/9
southern clump	PL	$4.0^\dagger$	$1.7 \pm 0.3$	$2.9 \pm 0.3$	$5.9 \pm 0.7$	2.9/9
2006						
northern clump	PL	$4.0^\dagger$	$1.6 \pm 0.07$	$15.2 \pm 0.4$	$28.7 \pm 0.7$	109/161
	PL	$3.8 \pm 0.3$	$1.5 \pm 0.14$	$15.5 \pm 0.4$	$27.4 \pm 0.7$	108/160
	Bremss.	$4.0^\dagger$	$13^{+4}_{-2}$	$14.5 \pm 0.4$	$26.5 \pm 0.7$	112/161
northern clump 1	PL	$4.0^\dagger$	$1.5 \pm 0.1$	$6.6 \pm 0.3$	$11.6 \pm 0.5$	42/56
northern clump 2	PL	$4.0^\dagger$	$1.6 \pm 0.1$	$8.8 \pm 0.3$	$17.1 \pm 0.6$	43/56
inner jet	PL	$4.0^\dagger$	$1.7 \pm 0.2$	$2.1 \pm 0.1$	$4.3 \pm 0.2$	25/56
	PL	$4.6^{+1.0}_{-0.8}$	$2.0 \pm 0.4$	$2.0 \pm 0.1$	$5.2 \pm 0.3$	24/56
	PL	$4.0^\dagger$	$1.3 \pm 0.2$	$3.4 \pm 0.2$	$5.4 \pm 0.3$	28/56
outer jet	PL	$4.8^{+0.9}_{-0.8}$	$1.6^{+0.4}_{-0.3}$	$3.2 \pm 0.2$	$6.3 \pm 0.4$	26/55
	PL	$4.0^\dagger$	$1.5 \pm 0.2$	$2.7 \pm 0.2$	$4.8 \pm 0.3$	38/56
southern clump	PL	$3.4^{+1.0}_{-0.8}$	$1.3 \pm 0.4$	$2.8 \pm 0.2$	$4.4 \pm 0.3$	37/55
	Bremss.	$4.0^\dagger$	$18^{+20}_{-9}$	$2.6 \pm 0.2$	$4.6 \pm 0.3$	39/56

NOTE. —  $N_H$  is in the unit of  $10^{22} \text{ cm}^{-2}$ , the absorbed ( $f_{0.5-10}^{\text{abs}}$ ) and unabsorbed fluxes ( $f_{0.5-10}^{\text{unabs}}$ ) are in units of  $10^{-13} \text{ erg s}^{-1} \text{ cm}^{-2}$  in the 0.5-10 keV range. The uncertainties quoted are 90% confidence intervals.

$^\dagger$  – held fixed in the fit.